ingegneria sismica
International Journal of Earthquake Engineering
Anno XLIII - Num. 3 - 2026

Study on the Influence of Cross-Sectional Shape on the Seismic Performance of 3D-Printed Concrete Walls

Zechen Gong[1], *Bo Wang*[1,*] *and Qiang Pei*[1]

[1] Liaoning Key Laboratory of Disaster Prediction and Prevention of Complex Structural Systems, Dalian University, Dalian 116622, China

SUMMARY: *In order to reveal the regulation law of cross-sectional configuration on the seismic performance of 3D printed concrete walls, and to make up for the shortcomings of existing research that mainly focuses on monotonic loading and rare analysis of seismic differences under reciprocating loads, this study adopts a concrete damage plasticity model and a cohesive interface model to design three typical cross-sectional walls: hollow, inclined rib, and vertical rib. Two axial compression ratios of 0.1 and 0.2 are set, and displacement controlled reciprocating loading is used to compare and analyze the displacement ductility, stiffness degradation, energy dissipation capacity, skeleton curve, and failure mode of the wall. The experimental results show that under the same axial compression ratio, the ductility of ribbed walls is significantly better than that of hollow walls. When the axial compression ratio is 0.1, the ductility coefficients of vertical and inclined ribbed walls are increased by 19% and 11% respectively compared to hollow walls; When the axial compression ratio increases from 0.1 to 0.2, the ductility coefficient of the three types of walls decreases by 5% to 10%, the stiffness degradation rate slows down, the energy dissipation capacity improves, and the ultimate bearing capacity increases but the ultimate displacement decreases; The degree of damage decreases from high to low as follows: hollow wall>inclined rib wall>vertical rib wall. Research has shown that vertical rib sections have both printability and excellent seismic performance, and changes in axial compression ratio do not alter their impact on ductility.*

KEYWORDS: *3D printing; concrete Cross-sectional form; seismic performance Axial compression ratio; numerical simulation*

1 Introduction

As a revolutionary innovation in the construction industry [1], 3DPC technology has attracted widespread attention from the academic and engineering communities around the world due to its high efficiency [2], cost-effectiveness [3], environmental sustainability [4], and ability to manufacture complex geometric structures [5]. However, unlike traditional cast-in-place concrete, 3DPC structures are manufactured through layer-by-layer additive manufacturing processes. This results in a completely different internal structure and materials from the usual methods, leading to market differences in seismic performance. The performance of the wall as the main load-bearing component directly determines the safety margin of the entire structure during seismic activity [6]. At present, research on the mechanical properties of 3D printed concrete walls (3DPCW) both domestically and internationally mainly focuses on the compression and bending behavior under static monotonic loads, using "experimental testing

*yiyuefeixue@163.com
https://doi.org/10.65102/is20261244 Published: 10 June, 2026

and numerical simulation" to elucidate the failure mechanism.

Based on the cross-sectional geometry and load-bearing mechanism, researchers use cross validation of experiments and numerical simulations to reveal the control laws of cross-sectional structures on load-bearing capacity. For example, Tamrazyan et al. [7] combined finite element simulations to demonstrate that although planar walls have superior axial compression capabilities, the diagonal ribs in diamond shaped walls can effectively alter the load transfer path and delay out of plane buckling, thus verifying the coupling effect of "cross-sectional shape axial compression shear". Idriss&Owais [8] extended the cross-section to honeycomb, triangular, and lattice grids. Due to direct vertical force transfer, rectangular grids provide optimal compression performance, providing a geometric prototype for seismic ductility design. Regarding the flexural performance of walls, the comprehensive model simulation by Vitorino et al. [9] shows that due to weak interlayer bonding, the flexibility of 3DPCW is usually lower than that of traditional concrete walls with similar steel bars. At the same time, cracks tend to propagate along the printed layer, making the interfacial fracture energy a key parameter determining the flexural bearing capacity.

Although the presence of interlayer pores increases the dispersion of bearing capacity, Nerella et al.'s study on the interlayer performance of 3D printed concrete based on extrusion shows that optimizing printing process parameters such as layer thickness, printing speed, and interlayer time interval can control the interfacial porosity within a specific range, thereby significantly improving mechanical performance. Geng et al. revealed the anisotropic distribution characteristics of interface pores from the perspective of double-layer microstructure, indicating that targeted optimization of material rheology and process parameters can achieve directional control of interface porosity. Overall, carefully adjusting porosity rather than completely eliminating pores is an effective strategy for improving the structural performance of 3D printed concrete components [10]. Regarding the shear enhancement mechanism, Krelani et al. [11] used numerical simulations of three-dimensional solid interface coupling elements combined with parameter testing to show that with the increase of inclined ribs, the shear strength significantly increased, with a peak value of 0.4. Beyond this value, due to the concentration of interface stress, shear slip failure would occur.

Although the above results reveal the influence of cross-sectional and structural details on the bearing capacity and failure mode of 3DPCW, existing research is mainly based on monotonic loading (compression, bending) and has not fully explored the seismic differences of 3DPCW with different cross-sectional forms under cyclic loading. Therefore, this article designed three typical cross-sectional 3DPCWs and subjected them to low cycle reverse loading under two different axial compression ratios to investigate displacement ductility, stiffness degradation, and skeleton curves, providing reference for seismic design and engineering applications of 3D printed concrete structures.

2 Numerical Model and Loading Protocol

2.1 Wall Dimensions

Due to its fast construction speed and high printing accuracy, 3DPCW has been widely used in engineering structural design. However, changes in printing paths can lead to different mechanical and seismic behaviors, which has become an important issue of concern for many researchers. This article compares and analyzes the seismic performance of three representative cross-sectional forms, namely hollow walls, inclined rib walls, and vertical rib walls, under low cycle repeated cyclic loads. According to the Code for Design of Concrete Structures (GB/T 50010-2010) [12] and the Technical Specification for Precast Concrete Structures (JGJ 1-2014)

[13], the minimum thickness of the 3DPCW is deter-mined to be 160 mm. This dimension satisfies the requirements for the minimum lap length of floor slabs on walls (70 mm) and the thickness of horizontal wall joints (20 mm). Furthermore, based on the Standard for Test Method of Basic Mechanics Proper-ties of Masonry (GB/T 50129-2011) [14], the aspect ratio (height-to-thickness ratio) of the specimen is controlled within the range of 3–5. Therefore, the wall dimensions are defined as 600 mm × 160 mm × 480 mm. The parameters of the three designed wall types with different cross-sections are illustrated in Figure 1.

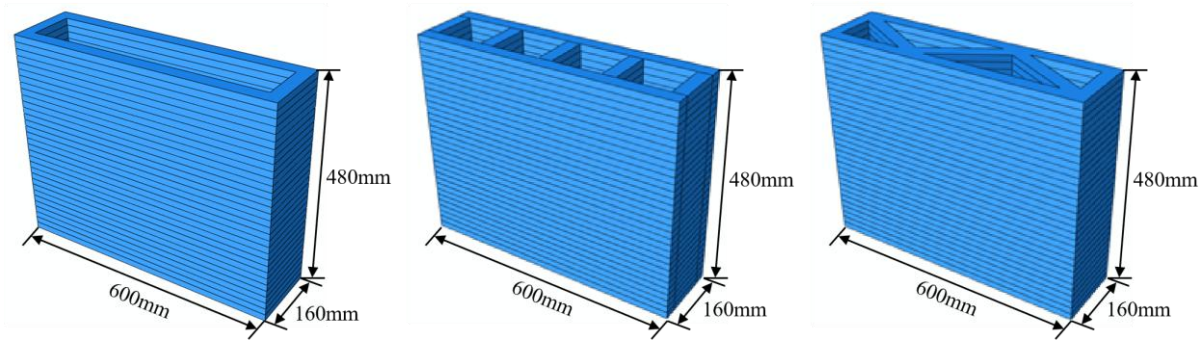

(a) (b) (c)

Figure 1: Wall design scheme: (a) Hollow wall; (b) Diagonally ribbed wall; (c) Vertically ribbed wall.

Taking into account the characteristics of the 3D printing process, the concrete printing layers were first modeled as individual components, which were then assembled into the complete wall structure according to the design specifications. To ensure high-accuracy meshing for the 3DPCW model in subsequent analyses, thereby enabling a more precise capture and simulation of the structural wall's mechanical behavior and response, the walls were simulated using eight-node linear hexahedral elements (C3D8). The seed spacing for the loading beam and ground beam elements was set to 80 mm, resulting in a mesh of 2,310 elements. For the 3D printed wall elements, a seed spacing of 30 mm was applied, resulting in 1,472, 2,112, and 1,824 elements for the hollow, diagonally ribbed, and vertically ribbed walls, respectively. Figure 2 illustrates the wall models after mesh generation.

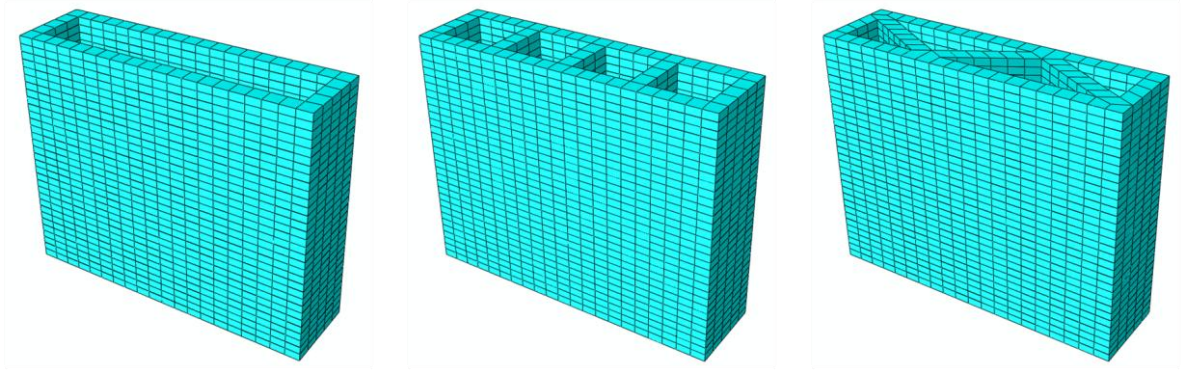

(a) (b) (c)

Figure 2: Wall model after meshing: (a) Hollow wall; (b) Diagonally ribbed wall; (c) Vertically ribbed wall.

2.2 Material Parameters

The concrete damage plasticity (CDP) model is generally considered the simplest and most accurate model available for simulating 3DPC structures, as its anisotropic damage, cyclic degradation, and interaction characteristics are similar to those of 3DPC. For example, Cakiroglu et al. [15], Kim and Lee [16] used the CDP model to simulate 3DPCW, and the test results showed that the expected values of parameters such as peak load, initial stiffness, or terminal displacement of the algorithm model were distributed between 7% and 12%. Research has shown that the proposed 3DPC algorithm model can accurately capture the anisotropy, cyclic degradation, and interlayer failure issues of 3DPC. The plastic damage constitutive model used in this article is shown in Figure 3. The concrete strength grade of the wall model in the figure is C30, so the elastic modulus is considered to be 34500 N/mm ², Poisson's ratio is 0.2, divergence angle is 30 °, and eccentricity is 0. For the mechanical properties of interlayer interfaces in 3DPC, the adhesive tape model (CZM) can be used for analysis, and its effectiveness has been widely studied and confirmed. Mincigrucci et al. [17], Baek et al. [18], and Ramirez et al. [19] utilized the Cohesive model to reproduce interlayer peeling, shear slip, and skeleton curves of 3D printing walls, showing good agreement between simulation results and experimental failure modes. In this paper, we use the Cohesive Model to simulate the mechanical properties of the 3-D printed concrete interface.

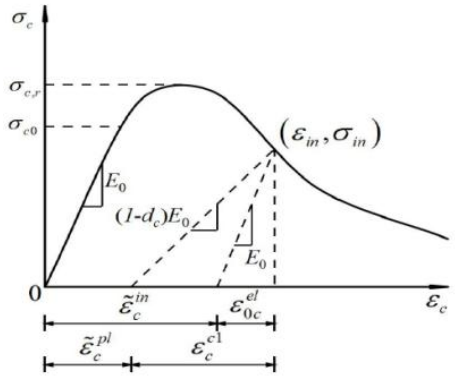

Figure 3: Stress-strain relationship of concrete.

2.3 Loading Method

The loading protocol was designed in accordance with the relevant provisions of the Specification for Seismic Test of Buildings (JGJ/T 101-2015) [20]. The simulation employed a displacement-controlled loading mode, with increments based on the initial yield displacement of the wall (Δy). A fully fixed boundary condition was applied to the bottom of the ground beam. The loading protocol consisted of two phases: first, monotonic loading under vertical dead load to determine Δy ; subsequently, the cyclic loading phase commenced, where the top displacement was increased step-by-step at amplitudes of $\pm 1\,\Delta y$,$\pm 2\,\Delta y$,$\pm 3\,\Delta y$, and so on. Each displacement amplitude included one full cycle (forward and backward), continuing until the bearing capacity dropped to approximately 85% of the peak load, which was defined as failure. The horizontal reciprocating displacement curve applied to the reference point on the side of the loading beam is shown in Figure 4. The maximum iteration number is set to 10000, the initial step size is set to 0.1, the minimum step size is set to 1 × 10-9, and the maximum step size is set to 0.5. Given that 3DPCW is typically a low-level structure, a low axial compression ratio was used in the simulation to ensure the safety and stability of the structure. For an axial compression ratio of 0.1, a vertical compressive force of 110.160 kN was applied through the

reference point at the top of the beam. For an axial compression ratio of 0.2, a vertical force of 220.320 kN was applied at the same location. For these vertical loading steps, the maximum number of iterations was set to 100, with an initial step size of 1, a minimum step size of 1×10^{-5}, and a maximum step size of 1. Table 1 presents the wall model schemes under the two axial compression ratios.

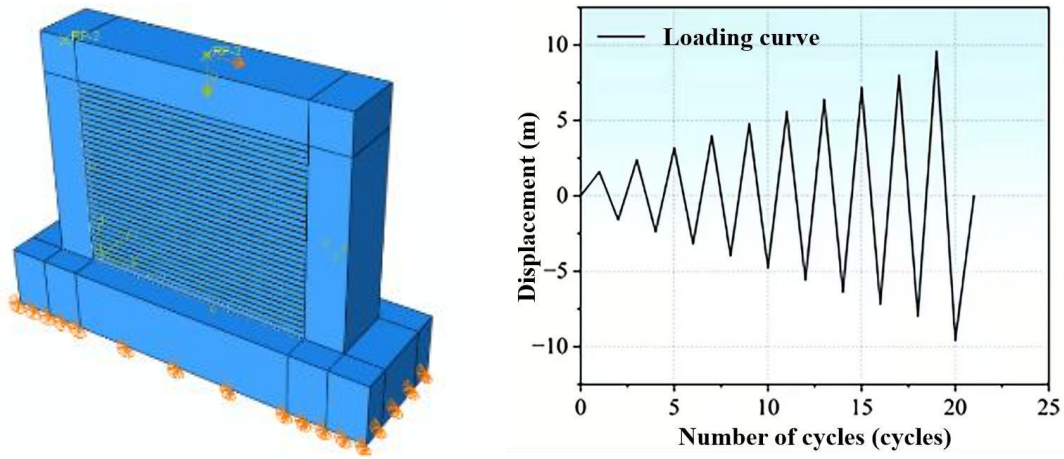

(a) (b)

Figure 4: Boundary conditions and loading protocol of the wall model: (a) Boundary conditions of the wall model; (b) loading protocol of the wall model.

Table 1: Wall model scheme.

Specimen No.	Axial compression ratio	Wall mode
W-1	0.1	Hollow wall
W-2	0.2	Hollow wall
W-3	0.1	Diagonal rib wall
W-4	0.2	Diagonal rib wall
W-5	0.1	Vertically ribbed wall
W-6	0.2	Vertically ribbed wall

2.4 Model Validation

Referring to the Test Method for Basic Mechanical Properties of 3D Printed Concrete (T/CBMF 183-2022) [21], an interlayer shear strength test was conducted on 3DPC with a C30 strength grade. The test employed displacement-controlled loading at a rate of 0.06 mm/min. The specimen dimensions were 40 mm × 100 mm × 120 mm, with the sampling direction parallel to the interlayer interface. The average interlayer shear strength measured from the test was 2.1 MPa. The Cohesive contact behavior adopted a quadratic stress failure criterion. Based on inverse analysis of the test results, the parameters were determined as follows: normal tensile strength of 1.5 MPa, shear strength in the first direction of 2.1 MPa, shear strength in the second direction of 2.1 MPa, and interfacial fracture energy of 0.15 N/mm. Figure 5 shows the schematic diagram of loading the shear specimen.

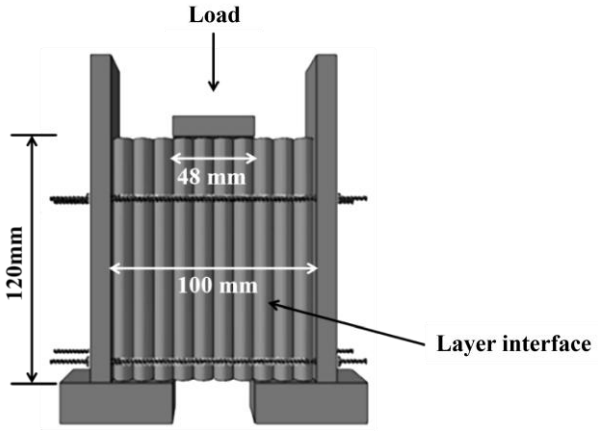

Figure 5: Schematic diagram of shear specimen loading.

The crack failure pattern of the specimen is shown in Figure 6. The cracks initiated from the upper or lower end of the printing layer where the strain gauges were attached. From there, the cracks propagated linearly either from top to bottom or from bottom to top, eventually forming splitting cracks that penetrated the entire specimen. The maximum crack width even reached 1-2 mm.

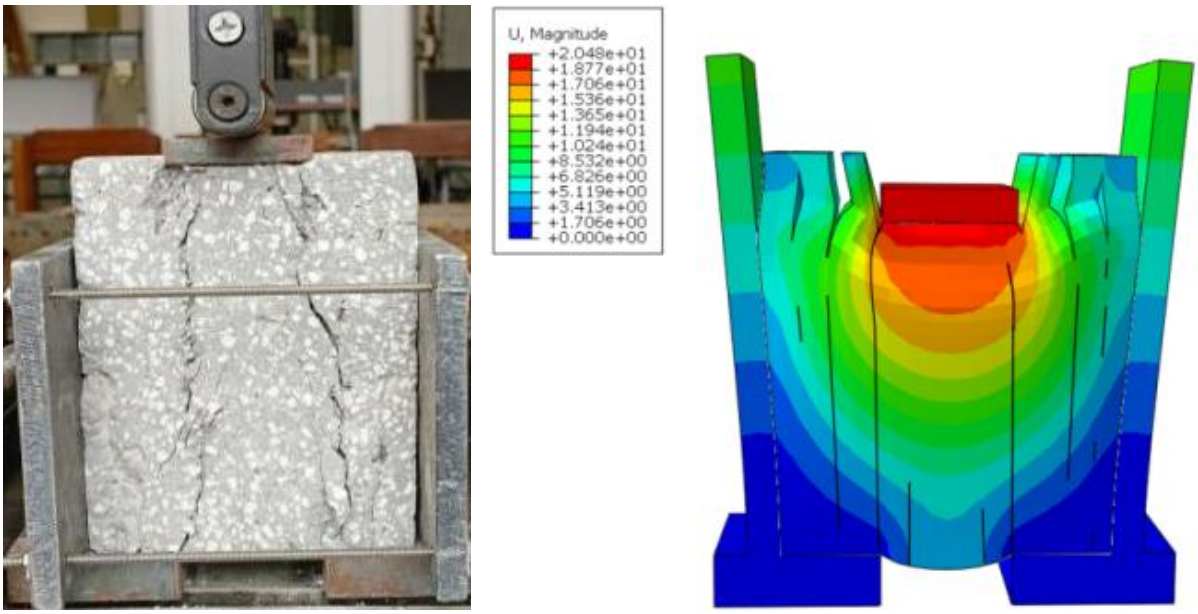

(a) (b)

Figure 6: Schematic diagram of crack failure pattern: (a) Experimental observation; (b) Simulation results.

Figure 6 (a) and figure 7 illustrate the crack failure patterns in the numerical simulation and the interlaminar damage nephograph, respectively. Comparing the experimental and simulated results, it is shown that the damage of the 3DPCstructure is well consistent with that of experiment. This confirms that the Cohesive model is applicable to the simulation of shear damage in 3DPC structures and further confirms the correctness of the following 3DPCW simulations.

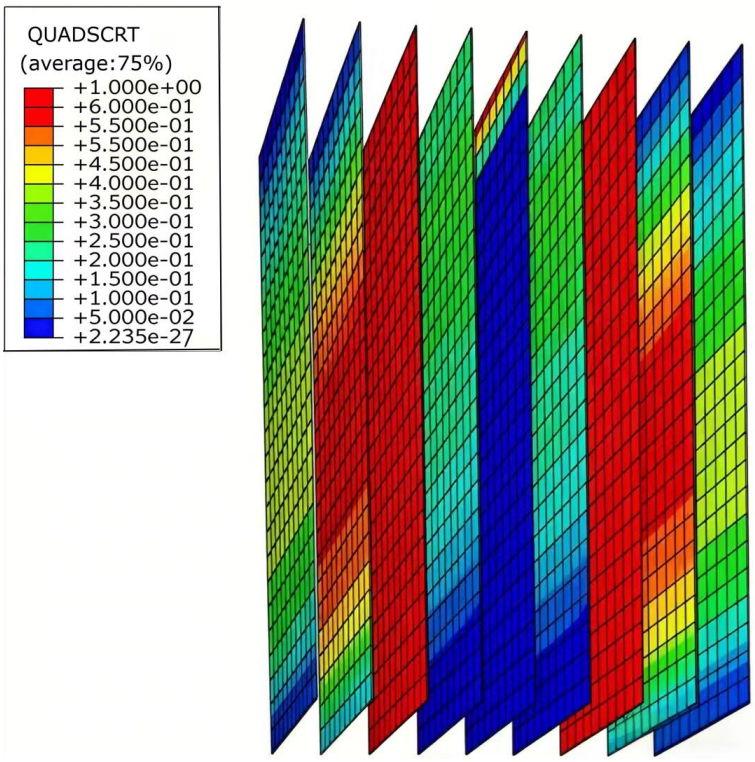

Figure 7: Interlayer damage nephogram of the shear test.

3 Results Analysis and Discussion

3.1 Displacement Ductility

Structural members with excellent ductility performance are capable of absorbing more seismic energy and undergoing larger deformations. This provides sufficient "buffer" space before the structure completely loses its load-bearing capacity. The ductility coefficient represents the quality of ductility development of a member under seismic action and can be calculated using Equation (1):

$$\mu = \Delta u / \Delta y \tag{1}$$

where: μ is the ductility coefficient; Δu is the ultimate horizontal displacement; Δy is the yield horizontal displacement.

To eliminate the difference in loading directions and obtain representative values, the arithmetic mean of the results from positive and negative loading is adopted. The calculated displacement ductility coefficients μ of 3DPCWs with different cross-sections are listed in Table 2.

Table 2: Ductility coefficient of wall.

Specimen	Loading direction	Yield load (kN)	Yield displacement (mm)	Ultimate load (kN)	Ultimate displacement (mm)	μ
W-1	Positive	60.75	0.93	61.43	3.36	3.61
	Negative	61.54	0.87	64.11	3.23	3.68
	Average	61.14	0.90	62.77	3.29	3.64
W-2	Positive	84.56	0.83	85.22	2.92	3.50
	Negative	81.93	0.91	84.65	2.91	3.18
	Average	83.25	0.87	84.94	2.91	3.34
W-3	Positive	97.54	1.28	96.25	4.98	3.86
	Negative	100.99	1.12	104.97	4.71	4.18
	Average	99.27	1.20	100.61	4.85	4.02
W-4	Positive	100.18	1.08	100.89	4.11	3.78
	Negative	102.53	1.09	105.46	3.90	3.57
	Average	101.35	1.09	103.17	4.01	3.67
W-5	Positive	132.53	1.55	139.73	6.47	4.15
	Negative	135.82	1.43	143.15	6.45	4.49
	Average	134.18	1.49	141.44	6.46	4.32
W-6	Positive	159.14	1.38	145.72	5.29	3.83
	Negative	140.81	1.15	159.46	5.09	4.39
	Average	149.98	1.26	152.59	5.19	4.11

3.2 Stiffness Degradation

Stiffness degradation is a direct manifestation of cumulative damage. If a wall experiences stiffness degradation, it indicates a gradual decrease in its ability to resist deformation under repeated loading. For 3DPCW, a slower rate of stiffness degradation indicates that interlayer bonding and internal structure can better maintain structural integrity and energy dissipation, resulting in excellent seismic performance. The stiffness degradation calculation model is as follows:

$$K_i = \frac{|+F_i| + |-F_i|}{|+X_i| + |-X_i|} \tag{1}$$

where: $+F_i, -F_i$ are the load value (kN) at the i-th positive and negative peak points; $+X_i$, $-X_i$ are the displacement value (mm) at the i-th positive and negative peak points.

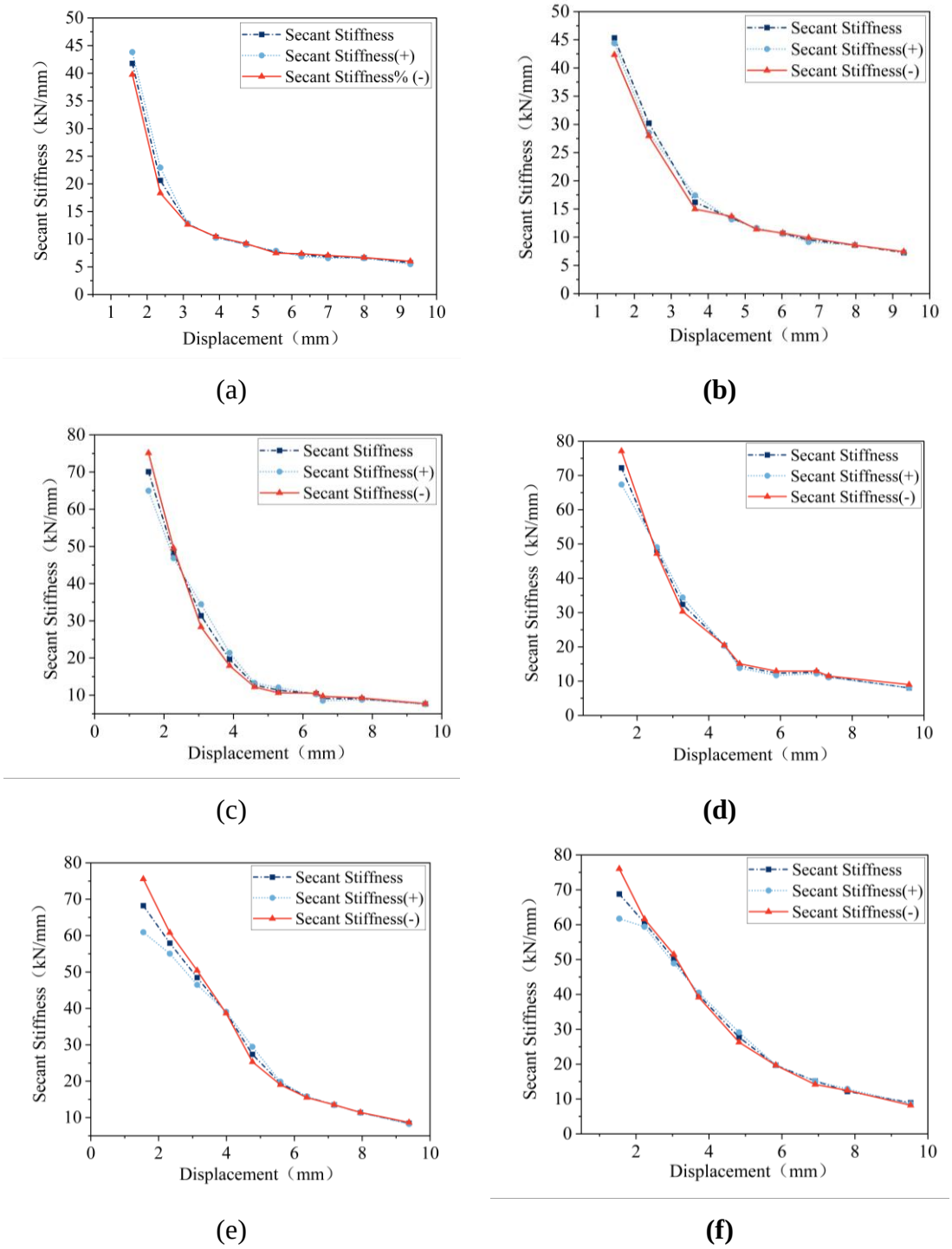

Figure 8: Stiffness degradation curves: (a) W-1; (b) W-2; (c) W-3; (d) W-4; (e) W-5; (f) W-6. Note: The horizontal axis represents the cyclic peak displacement Δ (mm), and the vertical axis represents the secant stiffness (kN/mm) corresponding to the cycle.

Figure 8 illustrates the stiffness degradation curves of various cross section 3DPCWs. Comparing the results of W-1 and W-2, W-3 and W-4, as well as W-5 and W-6, it is found that an appropriate increase in the axial compression ratio can effectively slow down the stiffness degradation rate of the walls. This is mainly reflected in the better stiffness retention during the early loading stage. However, the ductility of specimens with a high axial compression ratio is slightly reduced (Table 2), indicating that a slower stiffness degradation rate is not equivalent

to an improvement in ductility. This is because a higher axial compression ratio increases the friction between the printed layers, restricting crack development, thereby enhancing the overall stiffness of the wall and prolonging its retention time. Meanwhile, it also exacerbates the crushing and shear slip in the middle and lower parts of the wall limbs, leading to an earlier occurrence of the ultimate displacement.

3.3 Energy Dissipation Capacity

In seismic engineering, the energy dissipation capacity of a structure is considered one of the key factors influencing its seismic performance. The schematic diagram of energy dissipation coefficient calculation is shown in Figure 9. Evaluating the energy dissipation capacity of a structure helps to understand the energy absorption efficiency of the structural system under seismic loads. Relevant standards, such as the Standard for Seismic Test of Buildings (JGJ/T 101-2015) [22], provide the calculation method for the energy dissipation coefficient E, as shown in Equation (3).

$$E = \frac{S_{ABC} + S_{CDA}}{S_{OBE} + S_{ODF}} \tag{2}$$

where: $S_{ABC} + S_{CDA}$ is the area of the hysteretic loop, representing the total energy dissipated; $S_{OBE} + S_{ODF}$ is the sum of the areas of the two triangles OBE and ODF, representing the elastic energy of the component.

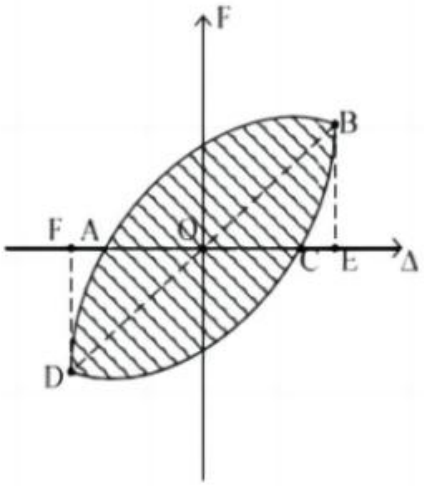

Figure 9: Schematic diagram of the calculation of the energy dissipation coefficient.

The energy dissipation coefficient curves of 3DPCWs with different cross-sectional shapes are shown in Figure 10. It can be observed that the energy dissipation coefficients of the hollow and diagonally cross-sectioned walls underwent two stages of decline: the first was a slow decrease after specimen failure, followed by a gradual recovery; the second was a sharp drop after yielding, after which the recovery rate accelerated, indicating a rapidly enhancing energy dissipation capacity of the walls. In contrast, the wall with vertical ribs exhibited a high energy absorption capacity under horizontal cyclic loading. Once entering the elasto-plastic stage, even when severely damaged, it could dissipate more energy through more sufficient plastic deformation, manifested by an increase in the area of the hysteretic loops and a rise in the energy dissipation coefficient [23].

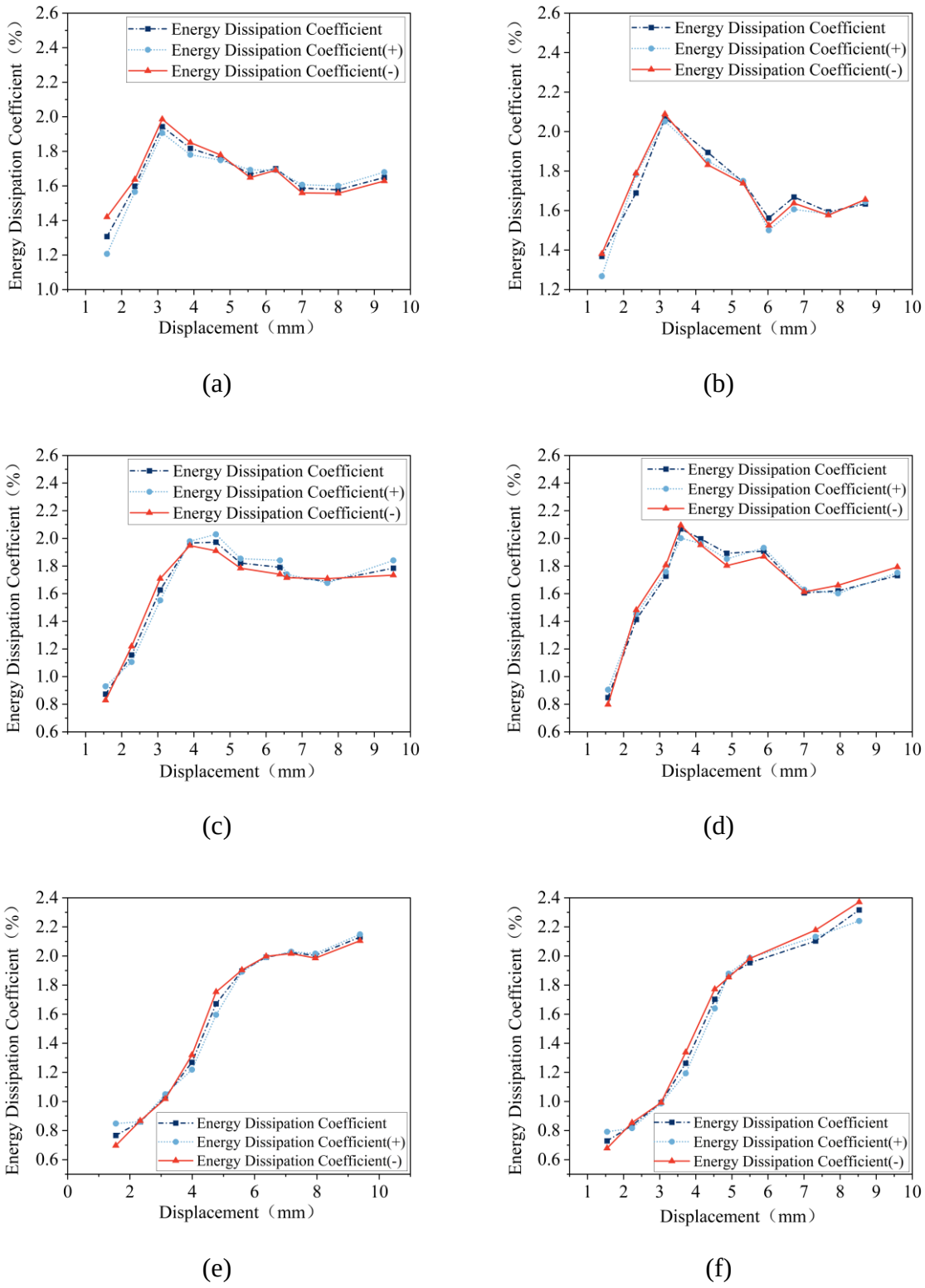

Figure 10: Energy dissipation coefficient curves: (a) W-1; (b) W-2; (c) W-3; (d) W-4; (e) W-5; (f) W-6.

3.4 Skeleton Curves

Figure 11 shows the skeleton curves of a 3DPW model with three different cross-sections. Analyzing the trend of the curve changes, it can be concluded that: (1) in the initial loading

stage, the sample is in the elastic deformation stage, showing a linear relationship. (2) After reaching the ultimate load, the curve shows obvious elastic characteristics, with slow growth of bearing capacity accompanied by significant deformation and damage, while still maintaining a certain bearing capacity; (3) When reaching the peak, the bearing capacity gradually decreases, but the remaining bearing capacity is retained [24].

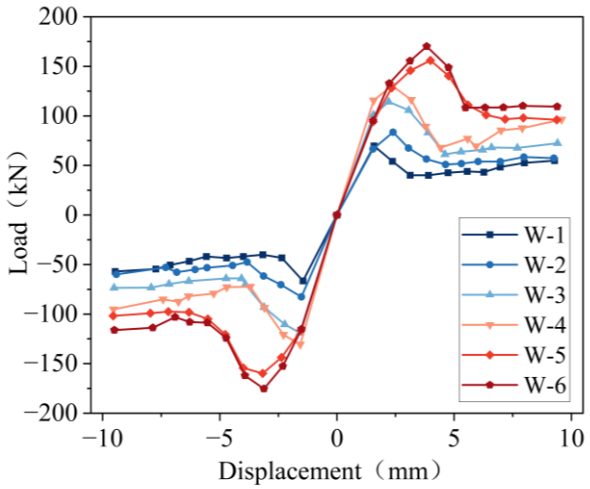

Figure 11: Skeleton curves.

The maximum bearing capacity of hollow walls is the lowest, mainly because hollow walls lack internal support structures, resulting in lower deformation resistance. Compared with hollow walls (W-1, W-2), walls with diagonal or vertical ribs (W-3, W-4, W-5, W-6) have higher load-bearing capacity, attributed to the additional shear resistance provided by the connecting rods, effectively delaying the occurrence of wall structural failure. In addition, by comparing the skeleton curves of wall models with different axial compression ratios (W-1 and W-2, W-3 and W-4, W-5 and W-6), it was found that increasing the axial compression ratio significantly improves the final bearing capacity of the wall, but leads to a decrease in peak displacement, reflecting the limited impact of increased stiffness on deformation capacity.

3.5 Failure Modes

The compressive damage contours (DAMAGEC) of 3DPCWs with different cross-sectional shapes under different axial compression ratios subjected to horizontal cyclic loading are shown in Figure 12. The darker areas in the figure correspond to the parts of the wall models with severe damage. It can be seen that the damage generated by the wall models under horizontal cyclic loading is mainly concentrated in the middle and lower parts of the walls, while the upper parts remain in a relatively intact state. Comparing the contour results of W-1, W-3, and W-5, it can be found that the severity of damage to the wall models follows the order: hollow wall > diagonal rib wall > vertical rib wall. Through the comparison of W-1 and W-2, W-3 and W-4, as well as W-5 and W-6, it is also observed that models W-2, W-4, and W-6 exhibit more severe damage compared to models W-1, W-3, and W-5. This is mainly caused by the greater pressure exerted on the walls. Although an increase in the axial compression ratio can enhance the bearing capacity of the walls, it also implies that when the loading exceeds a certain limit, the damage to the walls will be more severe.

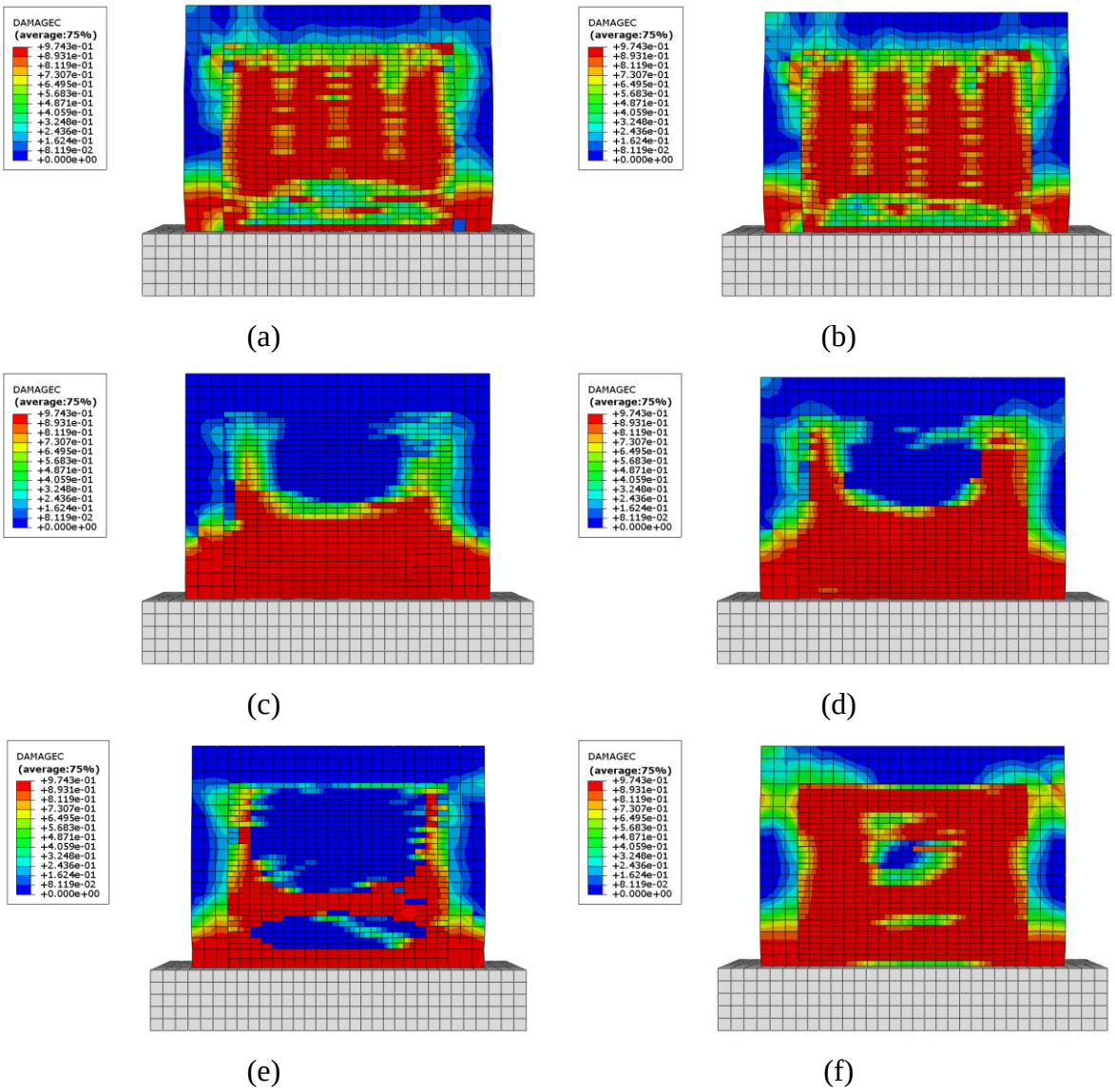

Figure 12: Damage contours of the walls: (a) W-1; (b) W-2; (c) W-3; (d) W-4; (e) W-5; (f) W-6.

4 Conclusions

Based on the numerical simulation analysis of 3DPCWs with three different cross-sectional shapes subjected to low-cycle reciprocating loading under different axial compression ratios, the main conclusions are as follows:

(1) Under the same axial compression ratio, the displacement ductility of the two types of walls with connecting ribs is significantly superior to that of the hollow wall. Taking an axial compression ratio of 0.1 as an example, the average displacement ductility coefficients μ for the hollow wall, diagonal rib wall, and vertical rib wall are 3.64, 4.02, and 4.32, respectively. The ductility of the diagonal rib wall and vertical rib wall is improved by approximately 11% and 19% compared to the hollow wall, respectively. Among them, the vertical ribs are continuously arranged along the height, providing both "boundary column confinement" and "integral stiffening" effects, enabling the wall piers to maintain good deformation capacity even after entering the elasto-plastic stage, thus showing the largest improvement in ductility.

(2) Within the range of axial compression ratios considered in this study (0.1–0.2), an increase in the axial compression ratio results in a "slight decrease" in the ductility of 3D printed concrete walls. As the axial compression ratio increases from 0.1 to 0.2, the displacement ductility coefficients of the three types of walls generally decrease by approximately 5%–10%. This is because 3D printed walls exhibit distinct weak interlayer interfaces and printing defects; a higher axial compression ratio exacerbates crushing in the middle and lower parts of the wall piers and leads to the premature occurrence of shear slip, thereby reducing the ultimate displacement. In traditional cast-in-place reinforced concrete members, the axial compression ratio is negatively correlated with ductility, and limiting the axial compression ratio is an important measure to ensure ductility.

(3) Based on the damage profile, it is found that the damage of the hollow wall is the most serious, the second is the diagonal, and the vertical rib is the least. With the increase of the axial compression ratio, the damage severity of the three cross section walls is also increased, which is due to the higher pressure applied to the wall. While increasing the axial compression ratio may increase the bearing capacity of the walls, it also implies that the damage to the walls will be more severe if the load exceeds a certain limit.

The above results indicate that introducing vertical ribs in 3DPCWs is a cross-sectional structural measure that offers advantages in both printability and seismic performance. It should be noted that this study still has certain limitations: First, the numerical model only verified the interfacial constitutive relationship through interlayer shear tests and did not perform experimental verification of the overall wall hysteretic performance. Second, the study adopted a low range of axial compression ratios (0.1–0.2); future research needs to expand to higher axial compression ratio ranges (0.3–0.6) to approach engineering practice. Additionally, the influence of material anisotropy caused by the printing path direction on the seismic performance of the walls was not considered. Subsequent work will conduct in-depth research and experimental verification targeting these aspects.

Author Contributions

Conceptualization, Q.P. and B.W.; methodology, Q.P.; software, Z.G.; validation, Z.G.; formal analysis, Z.G.; investigation, Q.P.; data curation, Z.G.; writing—original draft preparation, Z.G.; writing—review and editing, Q.P. and B.W.; visualization, Z.G.; supervision, Q.P. and B.W.; project administration, B.W.; funding acquisition, Q.P. All authors have read and agreed to the published version of the manuscript.

Funding

This research was funded by Dalian University, grant number 202301ZD01; Dalian Science and Technology Innovation Fund, grant number 2023JJ12GX012; and Liaoning Provincial Key Research and Development Plan, grant number 2019JH8/10100091.

Data Availability Statement

All data generated in this study are included in this paper. Raw data (including finite element model files and simulation result datasets) are available upon reasonable request from the corresponding author. Data sharing complies with MDPI’s data availability policy.

Acknowledgments

The authors would like to thank the reviewers and editors for their constructive feedback, which was crucial for the improvement of this paper. We gratefully acknowledge the funding support received from Dalian University, the Dalian Science and Technology Innovation Fund, and Liaoning Provincial Key Research and Development Plan for this study.

Conflicts of Interest

The authors declare no conflicts of interest.

References

[1] Tamrazyan A, Matseevich T. Seismic resistance of reinforced concrete building frames based on interval assessment of the coefficient of permissible damage[J]. Buildings, 2024, 14(12): 3776.

[2] Hassan A, Zhang C. Dynamic and static behaviour of geopolymer concrete for sustainable infrastructure development: Prospects, challenges, and performance review[J]. Composite Structures, 2025, 359: 118984.

[3] Ashot T, Vladimir C. Experimental and theoretical studies of seismic resistance parameters of reinforced concrete columns damaged by fire[J]. Structural Concrete, 2025, 26(4): 4814-4833.

[4] El-Joukhadar N, Dameh F, Pantazopoulou S. Seismic modelling of corroded reinforced concrete columns[J]. Engineering Structures, 2023, 275: 115251.

[5] Rezaie S, Khalighi M, Bahrami J, et al. On the integration of inspection data with seismic resilience assessment of corroded reinforced concrete structures[J]. Engineering Structures, 2024, 308: 117974.

[6] Saad A G, Sakr M A, Khalifa T M, et al. Structural performance of concrete reinforced with crumb rubber: A review of current research[J]. Iranian Journal of Science and Technology, Transactions of Civil Engineering, 2025, 49(4): 3211-3254.

[7] Tamrazyan A G, Matseevich T A, Savin S Y, et al. Seismic resistance of reinforced concrete columns under combined special actions[J]. Journal of Mechanics of Continua and Mathematical Sciences, 2025, 20(9): 52-72.

[8] Idriss L K, Owais M. Global sensitivity analysis for seismic performance of shear wall with high-strength steel bars and recycled aggregate concrete[J]. Construction and Building Materials, 2024, 411: 134498.

[9] Vitorino H, Real P V, Couto C, et al. Parametric analysis of post-earthquake fire resistance of reinforced concrete frames without seismic design[J]. Engineering Structures, 2024, 303: 117556.

[10] Lotfi V, Jahanitabar A A. Seismic resistance of concrete arch dams including contraction

joints based on damage plasticity model[J]. Multidiscipline Modeling in Materials and Structures, 2025, 21(3): 541-569.

[11] Krelani V, Ahmeti M, Kryeziu D. Increased durability of concrete structures under severe conditions using crystalline admixtures[J]. Buildings, 2025, 15(3): 352.

[12] Aljaafreh A, Alzubi Y, Al-Kharabsheh E, et al. Seismic performance of reinforced concrete structures with concrete deficiency caused by in-situ quality management issues[J]. Civ Eng J, 2023, 9(8): 1957-1970.

[13] Maidi M, Lifshitz Sherzer G, Shufrin I, et al. Seismic resilience of CRC-vs. RC-Reinforced buildings: A Long-Term evaluation[J]. Applied Sciences, 2024, 14(23): 11079.

[14] Gul A, Khan K, Khan I U, et al. Improving the lateral load resistance capacity of cellular lightweight concrete (CLC) block masonry walls through ferrocement overlay[J]. Applications in Engineering Science, 2024, 18: 100180.

[15] Cakiroglu C, Islam K, Bekdaş G, et al. Explainable machine learning models for predicting the axial compression capacity of concrete filled steel tubular columns[J]. Construction and Building Materials, 2022, 356: 129227.

[16] Kim M S, Lee Y H. Seismic performance of reinforced concrete columns retrofitted with hybrid concrete jackets subjected to combined loadings[J]. Materials, 2022, 15(18): 6213.

[17] Mincigrucci L, Civera M, Lenticchia E, et al. Comparative structural analysis of GFRP, reinforced concrete, and steel frames under seismic loads[J]. Materials, 2023, 16(14): 4908.

[18] Baek E, Pohoryles D A, Kallioras S, et al. Innovative seismic and energy retrofitting of wall envelopes using prefabricated textile-reinforced concrete panels with an embedded capillary tube system[J]. Engineering Structures, 2022, 265: 114453.

[19] Ramirez Ortiz C, Areiza Palma G, Gutierrez Amador A D, et al. Seismic behavior of a steel beam-to-concrete-filled steel tubular column connection using external diaphragms[J]. Applied Sciences, 2022, 12(7): 3618.

[20] Ensebekov A E, Alieva D K, Kydyrova Z D, et al. Study on seismic resistance and isolation method of concrete frame structure[J]. Architecture. Construction, 2024, 1(1): 106-114.

[21] Çelebi E, Kırtel O. Seismic performance of reinforced concrete framed buildings with ribbed slabs at the affected region by 2023 Kahramanmaraş earthquakes[J]. Bulletin of Earthquake Engineering, 2025, 23(9): 3623-3646.

[22] Kumar R, Dev N. Assessment of mechanical and impact resistance properties of rubberized concrete after surface modification of rubber crumb[J]. Iranian Journal of Science and Technology, Transactions of Civil Engineering, 2022, 46(4): 2855-2871.

[23] Merabti S, Guelmine L, Kaci M. Parametric analysis of the seismic behavior of reinforced concrete shear walls in buildings: application of the pushover method[J]. Revista Romana

de Materiale, 2025, 55(2): 124-134.

[24] Nishimura S, Tatsuki S, Kobayashi M, et al. Seismic-induced damage and restoration of rigid-frame reinforced concrete abutments for high-speed trains[J]. Engineering Structures, 2025, 327: 119598.